Turbulent drag reduction in water-lubricated channel flow of highly viscous oil

Alessio Roccon ⬤, Francesco Zonta ⬤,* and Alfredo Soldati ⬤
Institute of Fluid Mechanics and Heat Transfer, TU-Wien, 1060 Vienna, Austria
and Polytechnic Department, University of Udine, 33100 Udine, Italy

We study the problem of drag reduction (DR) in a lubricated conduit, in which a thin layer of low-viscosity (e.g., water) fluid is injected in the near-wall region and facilitates the transport of a core of high-viscosity fluid (e.g., oil). In the present investigation, the flow instance is a channel flow, and consequently we have one thin layer of low-viscosity fluid lubricating each wall. We run direct numerical simulations of this flow instance, respecting the protocol of the constant power input approach. This approach prescribes that the flow rate is adjusted according to current pressure gradient, so to keep constant the power injected into the flow, it mimics closely real transport pipelines. A phase-field method is used to describe the dynamics of the liquid-liquid interface. As this technique is tailored toward the transport of very viscous fluids like oils, we study the drag reduction performance of the system by keeping fixed the lubricating fluid properties (e.g., water) and by considering two different types of oil characterized by different viscosities, 10 and 100 times more viscous than water, respectively. As in real instances the presence of impurities and surfactants—which act by locally reducing the local value of the surface tension—is inevitable, we consider, for each type of transported oil, a clean and a surfactant-laden interface. For all four tested configurations, we unambiguously show that significant DR can be achieved. Reportedly, compared to the single-phase case, we observe a reduction of the mean pressure gradient down to $p_x/p_{x,\mathrm{sp}} = 0.25$ for the largest viscosity oil. By analyzing the features of turbulence in the lubricating layer, and the close interaction with the perturbations induced by the oil-water interface deformation, we elucidate the physical mechanisms leading to DR and we underline the effects of viscosity ratios and of surfactants.

I. INTRODUCTION

Pipelines are the most straightforward and used system to transport heavy oil. However, due the very high viscosity, moving heavy oil is an extremely energy-intensive process and requires high pumping power [1]. To reduce the required pumping power and the corresponding operating cost, different drag reduction (DR) techniques have been developed and tested in the past, including DR by polymers, surfactants, and fibers, (which act to modify the rheological properties of the flow and thus the apparent viscosity [2–10]); DR by riblets and active wall oscillations (which act to modify the turbulence regeneration cycle [11–16]); or DR by injection of a low viscosity fluid (e.g., water) in the near-wall region of the pipeline, so that the wall friction, induced by the low-viscosity fluid in contact with the wall, is lower (so-called water-lubricated oil transport). Among the different DR techniques, the water-lubricated oil transport has emerged as one of the most promising. This

---

*Now at School of Engineering, Newcastle University, Newcastle upon Tyne NE1 7RU, United Kingdom.

technique takes advantage of the natural tendency of water to form a stable layer that remains in contact with the wall of the pipe and that lubricates the oil flow [17–19]. Although the cross section available to the oil is reduced, this technique is appealing because of its simplicity and low costs. Not surprisingly, the literature in the field of water-lubricated pipelining is vast [19,20] but is mostly limited to theoretical studies focused on the stability of the flow configuration [17,21–23] or to experimental studies measuring the overall. performance and effectiveness of this DR strategy [24–27]. Accurate measurements of the flow field near the walls and at the liquid-liquid interface remain challenging, mainly because of the unfavorable optical properties of the involved liquids (i.e., opacity of oils) [28–30]. In this context, accurate simulations can be considered valuable tools that, granting access to the entire flow field and to the corresponding liquid-liquid interface deformation, can be used to fully characterize the underlying physics. Due to the challenges associated with the description of turbulent multiphase flows [31–33], direct numerical simulations of lubricated channels and pipes have been performed only in recent years [34–39] and have shown the importance of viscosity and surface tension in selectively modulating turbulence, and in generating the observed drag reduction.

In our previous works [38–41], we analyzed a simplified, yet relevant, flow configuration in which a thin layer of a lubricating fluid is injected near the top wall of the channel, so as to favor the transportation of the primary fluid. In the present work, we extend our previous studies to a more practically relevant configuration by acting on three different aspects: (i) we consider the presence of a lubricating layer on both the top and bottom walls, hence resembling the core-annular flow configuration obtained in pipes; note that near-wall turbulence in pipes and channels (which is the main character in the generation of the flow resistance) is very similar, in spite of the existing geometrical difference; (ii) we consider a very large difference in viscosity between the two phases, up to a viscosity ratio $\lambda = \eta_o/\eta_w = 100$, thus mimicking the crude oil-water cases; and (iii) we also take into account the presence of impurities and surfactants, which are very often present in this kind of applications and act by locally reducing the interfacial tension and introducing tangential stresses at the interface.

In particular, we consider the flow of two immiscible fluids, heavy oil and water, inside a rectangular flat channel. The top and bottom parts of the channel are occupied by two thin lubricating layers of water having thickness h_w, density ρ_w, and viscosity η_w, while the core part of the channel is occupied by oil and has thickness h_o, density ρ_o, and viscosity η_o. To mimic a realistic heavy oil-water system, we consider two fluids with the same density ($\rho_w = \rho_o = \rho$) but different viscosities, so that a viscosity ratio $\lambda = \eta_o/\eta_w$ can be defined. As mentioned above, in nearly all cases of practical importance for this kind of flows, contaminants, impurities, and surfactants are commonly found at the interface between the two phases. Therefore, we consider both surfactant-free (clean) and surfactant-laden systems. The dynamics of the system is captured by coupling direct numerical simulation of the Navier-Stokes equations, used to describe the flow field, with a two-order parameter phase-field method, used to describe the shape and deformation of the interface and the concentration of surfactant [42–45]. Simulations are performed using a constant power input (CPI) framework [39,46] which means that the flow is driven imposing a constant amount of power—product between flow rate and pressure gradient—and thus adjusting the imposed pressure gradient to the actual flow rate. In the study of drag reduction, this aspect is very important aspect since the adoption of a CPI approach puts on a firmer and more objective ground the comparison among different drag reduction techniques [46].

The paper is organized as follows: In Sec. II we present the governing equations and the numerical approach. The main results of the simulations are illustrated in Sec. III: First, we characterize the interface deformation and the surfactant distribution and then we analyze the interplay between the interface dynamics and the turbulence activity in the water lubricating layers; in addition, we evaluate the effects of the interface-turbulence interactions in the drag reduction performance by looking at the behavior of the mean velocity, flow rate, and pressure gradient. Finally, conclusions are outlined in Sec. IV.

II. METHODOLOGY

We consider the flow of two immiscible fluids inside a rectangular flat channel. At the top and bottom walls, two thin water lubricating layers are used to favor the transport of a thicker central layer of heavy oil. To capture the dynamics of the system, we couple direct numerical simulation of the Navier-Stokes equations, used to describe the flow field, with a two-order-parameter phase-field method, used to describe the deformation of the oil-water interface and the surfactant concentration [33,42–45].

A. Phase-field modeling of interfacial phenomena

In the framework of the two-order-parameter formulation of the phase-field method here employed, two scalar order parameters are used to describe the shape of the interfacial waves and the surfactant concentration (when present). A first-order parameter, the phase field, ϕ, describes the shape and position of the interface. A second-order parameter, ψ, is used to describe the concentration of surfactant [47–49]. The dynamics of the phase-field variable and the surfactant concentration are described by two Cahn-Hilliard-like equations, which in dimensionless form read:

$$\frac{\partial \phi}{\partial t} + \mathbf{u} \cdot \nabla \phi = \frac{1}{\text{Pe}_\phi} \nabla^2 \mu_\phi, \tag{1}$$

$$\frac{\partial \psi}{\partial t} + \mathbf{u} \cdot \nabla \psi = \frac{1}{\text{Pe}_\psi} \nabla \cdot [\psi(1-\psi)\nabla \mu_\psi], \tag{2}$$

where $\mathbf{u} = (u_x, u_y, u_z)$ is the velocity vector, Pe_ϕ and Pe_ψ are the phase-field and the surfactant Péclet numbers, and μ_ϕ and μ_ψ are the corresponding chemical potentials. The two Péclet numbers are defined as follows:

$$\text{Pe}_\phi = \frac{u_\Pi h}{\mathcal{M}_\phi \beta}; \quad \text{Pe}_\psi = \frac{u_\Pi h \alpha}{\mathcal{M}_\psi \beta^2}, \tag{3}$$

where u_Π is the characteristic velocity [properly introduced and discussed later, Equation (15)], h is the channel half-height, $\mathcal{M}_\phi$ and $\mathcal{M}_\psi$ the phase-field and the surfactant mobilities, while α and β are positive constants used in the dimensionless procedure. From a physical point of view, the two Péclet numbers represent the ratio between the diffusive timescale, $h^2/(\mathcal{M}_\phi \beta^2)$ or $h^2\alpha/(\mathcal{M}_\psi \beta^2)$, and the convective timescale, h/u_Π.

The chemical potentials μ_ϕ and μ_ψ are defined as the functional derivative of a two-order-parameter Ginzburg-Landau free-energy functional. The free-energy functional accounts for the interfacial motion and the surfactant dynamic [45,47–49]. The resulting expressions of the chemical potentials are as follows:

$$\mu_\phi = \frac{\delta \mathcal{F}}{\delta \phi} = \phi^3 - \phi - \text{Ch}^2 \nabla^2 \phi, \tag{4}$$

$$\mu_\psi = \frac{\delta \mathcal{F}}{\delta \psi} = \text{Pi} \log\left(\frac{\psi}{1-\psi}\right) - \frac{(1-\phi^2)^2}{2} + \frac{\phi^2}{2E_x}. \tag{5}$$

From these expressions, the equilibrium profiles for the two order parameters can be derived; at equilibrium, μ_ϕ and μ_ψ are uniform in the entire domain and therefore:

$$\nabla \mu_\phi = \mathbf{0}; \quad \nabla \mu_\psi = \mathbf{0}. \tag{6}$$

Considering a planar interface located at $s = 0$ (with s the coordinate normal to the interface), an analytic solution can be derived for the two order parameters:

$$\phi_{\text{eq}}(s) = \tanh\left(\frac{s}{\sqrt{2}\text{Ch}}\right), \tag{7}$$

$$\psi_{\text{eq}}(s) = \frac{\psi_b}{\psi_b + \psi_c(\phi_{\text{eq}})(1-\psi_b)}, \tag{8}$$

where the auxiliary variable, ψ_c, is a function of the phase field, and is defined as follows:

$$\psi_c(\phi_{\text{eq}}) = \exp\left[-\frac{1-\phi_{\text{eq}}^2}{2\text{Pi}}\left(1-\phi_{\text{eq}}^2+\frac{1}{E_x}\right)\right]. \tag{9}$$

The phase-field variable is uniform in the bulk of the two phases ($\phi_{\text{eq}} = \pm 1$) and undergoes a smooth transition following a hyperbolic tangent profile throughout the thin transition layer. Similarly, the concentration of surfactant is uniform in the bulk of the two phases, $\psi_b = \psi_{\text{eq}}$ ($\phi = \pm 1$), and reaches its maximum value at the interface, $\psi_0 = \psi_{\text{eq}}$ ($\phi = 0$). The maximum value of the surfactant concentration, ψ_0, is determined by the surfactant parameters Pi and E_x and by the bulk surfactant concentration, ψ_b, as indicated by Eqs. (7) and (8).

B. Hydrodynamics

To describe the hydrodynamics of the multiphase system, the two Cahn-Hilliard-like equations are coupled with the Navier-Stokes equations. The presence of a surfactant-laden interface—and of the corresponding surface tension forces—is accounted for by introducing an interfacial term in the Navier-Stokes equations. Surface tension forces are here calculated adopting a geometrical approach [50]: The geometrical proprieties of the interface are evaluated using the Korteweg tensor [51] while an equation of state (EOS) is used to describe the surface tension reduction produced by the surfactant. Recalling that in the present study we consider two fluids with the same density ($\rho = \rho_o = \rho_w$) but different viscosity ($\eta_o \neq \eta_w$), continuity and Navier-Stokes equations can be written as follows:

$$\boldsymbol{\nabla} \cdot \mathbf{u} = 0, \tag{10}$$

$$\frac{\partial \mathbf{u}}{\partial t} + \mathbf{u} \cdot \boldsymbol{\nabla} \mathbf{u} = -\boldsymbol{\nabla}\Pi - \boldsymbol{\nabla} p + \frac{1}{\text{Re}_\Pi}\boldsymbol{\nabla} \cdot [\eta(\phi)(\boldsymbol{\nabla}\mathbf{u} + \boldsymbol{\nabla}\mathbf{u})] + \frac{3\text{Ch}}{\sqrt{8}\text{We}_\Pi}\boldsymbol{\nabla} \cdot [f_\sigma(\psi)\tau_c], \tag{11}$$

where p is the pressure field, $\boldsymbol{\nabla}\Pi = (p_x, 0, 0)$ is the mean pressure gradient that drives the flow, $\eta(\phi)$ is the viscosity map accounting for the viscosity contrast between the two phases [44], $f_\sigma(\psi)$ is the surface tension equation of state, and τ_c is the Korteweg tensor. The Korteweg tensor [51], used to account for the surface tension forces, is defined as follows:

$$\tau_c = |\boldsymbol{\nabla}\phi|^2\mathbf{I} - \boldsymbol{\nabla}\phi \otimes \boldsymbol{\nabla}\phi, \tag{12}$$

where $\mathbf{I}$ is the identity matrix. The interfacial term, composed by the equation of state and the Korteweg tensor, accounts for both the normal and the tangential components of the surface tension that arise when the surface tension is not uniform.

The EOS adopted in this work is a modified Langmuir equation. While at low surfactant concentrations the Langmuir EOS follows well the experimental measurements, there is experimental evidence for liquid-liquid [52,53] and gas-liquid systems [54] showing that the surface tension never decreases below about 30% to 60% of the clean interface surface tension for any surfactant concentration. This is a consequence of the saturation of the interface: Once a monolayer of surfactant molecules is formed on the interface, no more surfactant can accumulate there, and the surface tension remains constant [55]. However, the Langmuir EOS predicts an unbounded surface tension decrease as surfactant concentration increases. Thus, we use a modified EOS, in which the minimum surface tension value is set to half of the clean interface surface tension value [52–54]. The resulting EOS is as follows:

$$f_\sigma(\psi) = \frac{\sigma(\psi)}{\sigma_0} = \max\left[\underbrace{1 + \beta_s \log(1-\psi)}_{\text{Langmuir EOS}}, 0.5\right], \tag{13}$$

where $\sigma(\psi)$ is the dimensional surface tension of the surfactant-laden interface, σ_0 is the surface tension of a clean interface, and β_s the elasticity number. This latter parameter quantifies the strength of the surfactant: For a fixed concentration of surfactant, a higher surface tension reduction can be obtained with a stronger surfactant (higher β_s).

The dimensionless groups appearing in Eq. (11) are the power Reynolds number, Re_Π, and the Weber number, We_Π, which are defined as:

$$\mathrm{Re}_\Pi = \frac{\rho u_\Pi h}{\eta_w}, \quad \mathrm{We}_\Pi = \frac{\rho u_\Pi^2 h}{\sigma_0}. \tag{14}$$

The Reynolds number represents the ratio between inertial and viscous forces and is defined based on the viscosity of the two lubricating layers (water), η_w, while the Weber number is the ratio between inertial and surface tension forces. The Weber number is here defined using the surface tension of a clean interface, σ_0, as reference. These two dimensionless parameters, as well as the Péclet numbers, are defined employing u_Π (discussed below) as a velocity scale.

As anticipated, in the present work we employ the CPI approach [39,46,56], which is based on driving the flow by a constant pumping power, P_p. Naturally, to keep the pumping power constant over time, the mean pressure gradient is dynamically adjusted according with the overall flow rate, Q_t. Within the CPI approach, the following velocity is introduced as a reference:

$$u_\Pi = \sqrt{D}\sqrt{\frac{P_p h}{3\eta_w}}, \tag{15}$$

where, as stated above, η_w is the water viscosity (lubricating layers), while D is a coefficient used to account for the presence of a core layer with different viscosity in the central part of the channel. From a physical point of view, the characteristic velocity u_Π represents the bulk velocity (average velocity across the channel section) of the actual two-phase flow configuration (i.e., two immiscible fluid layers having different viscosity and flowing inside a channel under the action of a pumping power P_p) but in laminar conditions. When the viscosity of the two layers is the same (single-phase or $\lambda = 1$), the coefficient D is unitary and the characteristic velocity reduces to:

$$u_\Pi = u_\Pi^{\mathrm{sp}} = \sqrt{\frac{P_p h}{3\eta}}, \tag{16}$$

matching the standard definition of the reference velocity under CPI conditions [46], where η represents the viscosity of the system (which is uniform for a single-phase flow or for $\lambda = 1$). We refer the reader to Appendix for additional details.

C. Numerical method

The governing equations (1), (2), (10), and (11) are solved using a pseudospectral method based on transforming the field variables into wave-number space via a combination of Fourier series (in the periodic stream and span directions) and Chebyshev polynomials (in the inhomogeneous wall normal direction). The collocations points for all variables (velocity and phase field) are equally spaced along the x and y directions while they are stretched along the wall-normal direction where a finer grid resolution is obtained near the two walls. Navier-Stokes equations are solved using a wall-normal velocity-vorticity formulation [57,58]. In particular, Navier-Stokes equations are rewritten as a fourth-order equation for the wall-normal component of the velocity u_z and a second-order equation for the wall-normal component of the vorticity ω_z. In contrast, the phase-field and the surfactant concentration transport equations are directly solved in their original formulation. Further details on the method can be found in Soligo *et al.* [49].

The governing equations are advanced in time using a mixed implicit-explicit scheme. For the Navier-Stokes equations, the nonlinear diffusive term is first rewritten as the sum of a linear and a nonlinear contribution [40,41,59]. The linear part is then integrated using a Crank-Nicolson implicit

scheme while the nonlinear part, together with the nonlinear convective terms, is integrated using an Adams-Bashforth explicit scheme. For the two Cahn-Hilliard-like equations (phase-field and surfactant concentration), the linear terms are integrated using an implicit Euler scheme, while the nonlinear term are integrated in time using an Adams-Bashforth scheme. Together with the time advancement of the equations, also the applied mean pressure gradient is updated at each time step, so to keep constant the power injected into the system (for further details, see Roccon *et al.* [39]).

D. Boundary conditions

The governing equations are complemented by suitable boundary conditions. For the Navier-Stokes equations, no-slip boundary conditions are enforced at the top and bottom walls ($z/h = \pm 1$):

$$u_i(z/h = \pm 1) = 0. \tag{17}$$

For the phase field, surfactant concentration and the corresponding chemical potentials, no-flux boundary conditions are enforced at the two walls:

$$\frac{\partial \phi}{\partial z}(z/h = \pm 1) = 0; \quad \frac{\partial \mu_\phi}{\partial z}(z/h = \pm 1) = 0, \tag{18}$$

$$\frac{\partial \psi}{\partial z}(z/h = \pm 1) = 0; \quad \frac{\partial \mu_\psi}{\partial z}(z/h = \pm 1) = 0. \tag{19}$$

This is equivalent to imposing the following boundary conditions:

$$\frac{\partial \phi}{\partial z}(z/h = \pm 1) = 0; \quad \frac{\partial^3 \phi}{\partial z^3}(z/h = \pm 1) = 0; \quad \frac{\partial \psi}{\partial z}(z/h = \pm 1) = 0. \tag{20}$$

Along the streamwise and spanwise directions (x and y), periodic boundary conditions are implicitly applied for all variables. The adoption of these boundary conditions leads to the conservation of the two order parameters (phase-field and surfactant concentration) over time:

$$\frac{\partial}{\partial t} \int_\Omega \phi \, d\Omega = 0; \quad \frac{\partial}{\partial t} \int_\Omega \psi \, d\Omega = 0. \tag{21}$$

where Ω is the domain considered. For the phase field, this does not guarantee the conservation of the individual mass of the two phase, and some small leakages between the phases may occur [60–62]. In the present cases, the mass leakage is always below 1%.

E. Simulation setup

The computational setup consists of a plane channel with dimensions $L_x \times L_y \times L_z = 4\pi h \times 2\pi h \times 2h$. We run five different simulations: a reference simulation of a single-phase turbulent channel flow and four multiphase simulations of water-lubricated oil channel flow. As sketched in Fig. 1, for the water-lubricated cases, two lubricating layers, thickness $h_w = 0.15h$, are injected in the near-wall region of the channel, so to favor the transport of a central layer of oil, thickness $h_o = 1.7h$. All multiphase simulations consider water as lubricating fluid and oil—in one case 10 times more viscous than water (viscosity ratio $\lambda = \eta_o/\eta_w = 10$) and in the other case 100 times more viscous than water (viscosity ratio $\lambda = \eta_o/\eta_w = 100$)—as transported fluid. For each value of the viscosity ratio (i.e., type of oil), we perform the simulation of a clean system (constant and uniform surface tension) and a surfactant-laden system (surface tension depends on the local surfactant concentration). This strategy is followed to mimic what happens in the large majority of cases, in which oil and water are not pure, but carry small quantities of impurities and surfactants.

All simulations are performed injecting into the system the same power P_p (CPI approach). For the single-phase case, this leads to a Reynolds power number equal to $\mathrm{Re}_\Pi = 80\,000$ (which roughly corresponds to a shear Reynolds number $\mathrm{Re}_\tau = 1000$). For the water-lubricated cases, the resulting power Reynolds number is different due to the effective viscosity of the system (and thus different
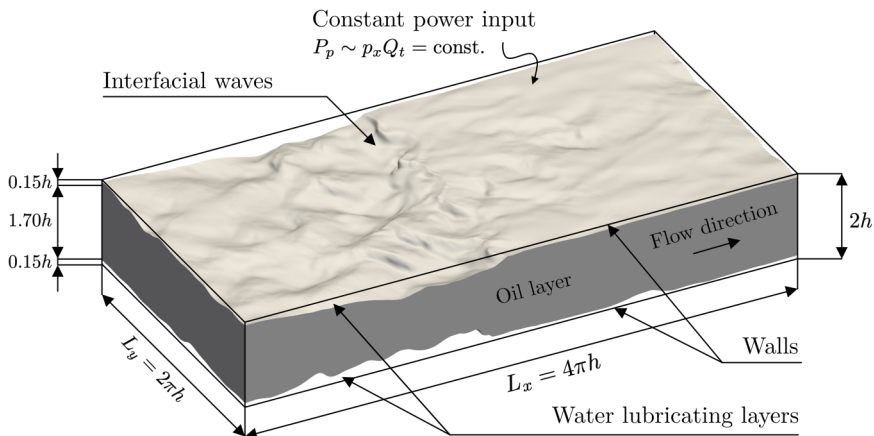
FIG. 1. Sketch of the flow and of the computational setup used for the simulations. Two near-wall lubricating layers of water (transparent), thickness $0.15h$, are used to favor the transport of a core layer of oil (gray), thickness $1.7h$, inside a channel. The channel has dimensions $L_x \times L_y \times L_z = 4\pi h \times 2\pi h \times 2h$. A constant power is injected into the system to drive the flow, which goes from left to right: the mean driving pressure gradient, p_x, is dynamically adjusted according to the instantaneous value of the volume flow rate, Q_t, so to keep constant the power (in physical units).

reference velocity u_Π). In particular, it ranges from $\text{Re}_\Pi = 53\,504$ for $\lambda = 10$ to $\text{Re}_\Pi = 50\,080$ for $\lambda = 100$. The surface tension value of the liquid-liquid interface is set via the Weber number so to be representative of an oil-water interface [63]. In particular, the Weber number is $\text{We} = 1431$ for $\lambda = 10$, while it is equal to $\text{We}_\Pi = 1254$ for $\lambda = 100$, because of the different characteristic velocity. For the two surfactant-laden cases, the elasticity number is $\beta_s = 1.00$, resembling the behavior of a surfactant with a moderate strength. An overview of the simulation parameters is reported in Table I.

Grid resolution is chosen to meet the requirements imposed by direct numerical simulations (DNS) and at the same time to guarantee a proper resolution of the thin interface between the two fluid layers and of the surfactant concentration field, see Table II. For the single-phase reference case, we use $N_x \times N_y \times N_z = 1024 \times 1024 \times 513$ grid points; for the surfactant-free cases, and because of the lower value of Re_Π, we use $N_x \times N_y \times N_z = 1024 \times 512 \times 513$; and finally, for surfactant-laden cases, we use $N_x \times N_y \times N_z = 2048 \times 1024 \times 513$ grid points. The Cahn number is set to $\text{Ch} = 0.01$ to allow an accurate description of the steep gradients present

TABLE I. Overview of the main simulation parameters. Five different cases have been considered: a single-phase case and four water-lubricated configurations, considering different values of the viscosity ratio ($\lambda = 10$ and $\lambda = 100$) and considering the presence (or not) of surfactants (clean vs surf. simulations). All simulations are performed driving the flow with the same pumping power P_p in physical units (CPI approach). For ease of comparison with literature results, the value of the shear Reynolds number (Re_τ) (computed *a posteriori*) is also reported.

System	λ	Re_Π	Re_τ	$\sqrt{D}$	We_Π	β_s	Ch	Pe_ϕ	ψ_b	Pe_ψ	Pi	E_x
Single-phase	—	80 000	1000	—	—	—	—	—	—	–	—	—
Multiphase (clean)	10	53 504	874	0.668	1431	—	0.01	16 050	—	—	—	—
Multiphase (surf.)	10	53 504	879	0.668	1431	1.00	0.01	16 050	0.01	5350	1.35	0.117
Multiphase (clean)	100	50 080	769	0.626	1254	—	0.01	15 024	—	—	—	—
Multiphase (surf.)	100	50 080	769	0.626	1254	1.00	0.01	15 024	0.01	5008	1.35	0.117

TABLE II. Summary of the grid resolution employed for the different cases. The grid spacing along the three directions is reported in wall units; for the wall-normal direction, where the grid is stretched, the grid spacing is reported and evaluated at the wall. The Kolmogorov length-scale (evaluated at the wall), $\eta_{k,w}^+$, is also reported.

System	λ	$N_x \times N_y \times N_z$	Δx^+	Δy^+	Δz_w^+	$\eta_{k,w}^+$
Single-phase	—	$1024 \times 1024 \times 513$	12.27	6.14	0.020	1.43
Multiphase (clean)	10	$1024 \times 512 \times 513$	10.72	10.72	0.017	1.51
Multiphase (surf.)	10	$2048 \times 1024 \times 513$	5.39	5.39	0.017	1.52
Multiphase (clean)	100	$1024 \times 512 \times 513$	9.43	9.43	0.015	1.80
Multiphase (surf.)	100	$2048 \times 1024 \times 513$	4.71	4.71	0.015	1.77

at the interface [61]. The phase-field Péclet number (i.e., the mobility) is chosen according to the scaling $\text{Pe}_\phi \propto 1/\text{Ch}$ [64], which gives an asymptotic convergence to the sharp-interface limit. The resulting Péclet number is $\text{Pe}_\phi \simeq 15\,000$ and changes only slightly with the considered viscosity ratio, because of the different characteristic velocity.

For surfactant-laden cases, the bulk concentration of the surfactant is kept fixed (in all cases) at $\psi_b = 0.01$, while the surfactant Péclet number is set to $\text{Pe}_\psi \simeq 5000$. This value can be considered representative of the behavior of nonionic and anionic surfactants in aqueous solutions [65]. The temperature-dependent parameter and the surfactant solubility parameter are set to $\text{Pi} = 1.35$ and $E_x = 0.117$, in agreement with previous works [45,49,66]. These parameters can be also set according to the specific type of surfactant considered. However, their values affect only the surfactant equilibrium profile and the bulk concentration while the main surfactant action (i.e., the surface tension reduction) is determined by the elasticity number. Hence, similar results (in terms of surface tension reduction) can be obtained changing these parameters together with the elasticity number. We choose here to fix these values according to previous studies and to set the elasticity number so that surface tension reductions commonly obtained in oil-surfactant-water systems are obtained [67].

For all simulations, the initial condition is taken from a preliminary DNS of a single-phase fully developed turbulent channel flow at $\text{Re}_\tau = 1000$ performed using a constant pressure gradient approach. The flow field is rescaled in CPI units, and the simulation is complemented by a proper definition of the initial phase-field distribution so that the two liquid-liquid interfaces are located at distance $h_w = 0.15h$ from the two walls (top and bottom), and the interfacial profile follows the hyperbolic tangent equilibrium profile, Eq. (7). When surfactant-laden cases are studied, the concentration is initialized with the surfactant equilibrium profile, Eq. (8).

The numerical scheme has been implemented in a parallel Fortran 2003 MPI in-house proprietary code. The parallelization strategy is based on a two-dimensional domain decomposition to divide the workload among all the MPI tasks. The solver execution can be offloaded to GPUs via OpenACC directives and CUDA Fortran instructions. Likewise, Fourier-Chebyshev transforms are performed using the FFTW libraries (CPU) or the Nvidia cuFFT libraries (GPU). Overall, the computational method adopted allows for the accurate resolution of all the governing equations and the achievement of an excellent parallel efficiency thanks to the fine-grain parallelism offered by the numerical method. The computational cost of the simulations is approximately 80 million CPU h and simulations have been performed on the Hawk supercomputer installed at the high-performance computing center located in Stuttgart, Germany (HLRS). All simulation runs have been performed using 64 or 128 computing nodes (64 for the smaller grid resolutions and 128 for the larger grid resolutions). The resulting dataset has a size of approximately 20 TB.

In the following, and for the sake of comparison against archival literature, results are presented in wall units (unless differently indicated), i.e., using u_τ as reference velocity, h as reference length, and h/u_τ as reference time. As the Reynolds number (both power and friction Reynolds number)

is different among the different cases, each case is normalized using its own value of u_τ. Angular brackets, $\langle \cdot \rangle$, are used to indicate the average in space and time.

III. RESULTS

Given the complexity of the problem, results will be discussed first by focusing on the qualitative structure of the flow and of the oil-water interface. Then these findings are used to provide a physically based explanation for the flow behavior observed in the lubricating layers, which we characterize by means of the wall-shear stress distribution. Finally, the drag reduction performances are quantified computing the behavior of the mean velocity, the flow rate and the pressure gradient. In the following, the results presented have been computed once a new statistically steady-state configuration is attained for all systems. Indeed, all simulations exhibit an initial transient where the flow adapts to the new configuration (water-lubricating layer and central core of oil). Once this new steady-state configuration is attained, statistics are computed using a time window of approximately $\Delta t^+ = 6000$.

A. Structure and deformation of oil-water interface

We start our discussion by looking at the flow field in the lubricating layers and at its connection with the behavior of the oil-water interface. We highlight that for the range of parameters here considered, no breakage of the interface is observed as the Weber number is below (or close to) the critical one for wave breaking [68]. Results are reported in Fig. 2. Figure 2(a) shows an instantaneous three-dimensional sketch of the oil-water interface (referring to the case $\lambda = 10$). In Figs. 2(b) and 2(c) we present a two-dimensional view from the top of the interface (for $\lambda = 10$ [Fig. 2(b)] and $\lambda = 100$ [Fig. 2(c)]) while in Figs. 2(d) and 2(e) we present the corresponding volume rendering of the turbulent kinetic energy, TKE $= (u_x'^2 + u_y'^2 + u_z'^2)/2$, in the bottom lubricating layer. As indicated in Fig. 2(a), the flow moves from left to right. Note that, because of the flow symmetry along z, a specular situation happens at the top wall.

First, we examine the effect of the viscosity ratio focusing on the two clean cases only ($\lambda = 10$ and $\lambda = 100$). Considering the case $\lambda = 10$ [Figs. 2(b) and 2(d)], we notice that the interface deformation is characterized by the streamwise and spanwise propagation of waves with different amplitude and wavelength, which interact and generate an highly irregular interface shape. We define crests as interface locations farther from the bottom wall (i.e., closer to the center of the channel) and troughs as interface locations closer to the bottom wall [see Fig. 2(a)]. As expected, the interface shape has a direct influence on the behavior of the flow field in the water lubricating layer [Fig. 2(d)]. In particular, where the interface has high crests and rough shape, turbulence seems to be active in the lubricating layer (see for example the turbulent spots in the region $\pi < x/h < 2\pi$); where the interface has deep troughs—and smoother shape—turbulence activity in the lubricating layer appears weak, since there is not enough room for the turbulence cycle to be sustained [69] and the flow tends to laminarize (see laminar patches in the region $2\pi < x/h < 3\pi$). Overall, this results into the coexistence of laminar and turbulent regions. These observations, which highlight the existing strong correlation between the the interface deformation and the turbulence activity, are consistent with previous investigations showing turbulence suppression and reactivation [38,39] depending on the local thickness of the lubricating layer. Considering the case $\lambda = 100$ [Figs. 2(c) and 2(e)], we notice that the interface is smoother and more regular. Given the relatively smaller interface deformation, crests and trough are now less pronounced, indicating a more uniform, and turbulent, flow field in the lubricating layer [Fig. 2(e)]. We also note that some modulation of the TKE activity is possible and can generate localized laminar patches, but the characteristic size of these laminar patches is much smaller compared to $\lambda = 10$.

To quantify the deformation of the oil-water interface, we compute the probability density function (PDF) of the interface elevation, ζ/h, i.e., the difference between the instantaneous interface position and the nominal interface position (located at a distance $z/h = 0.15$ from the walls). The
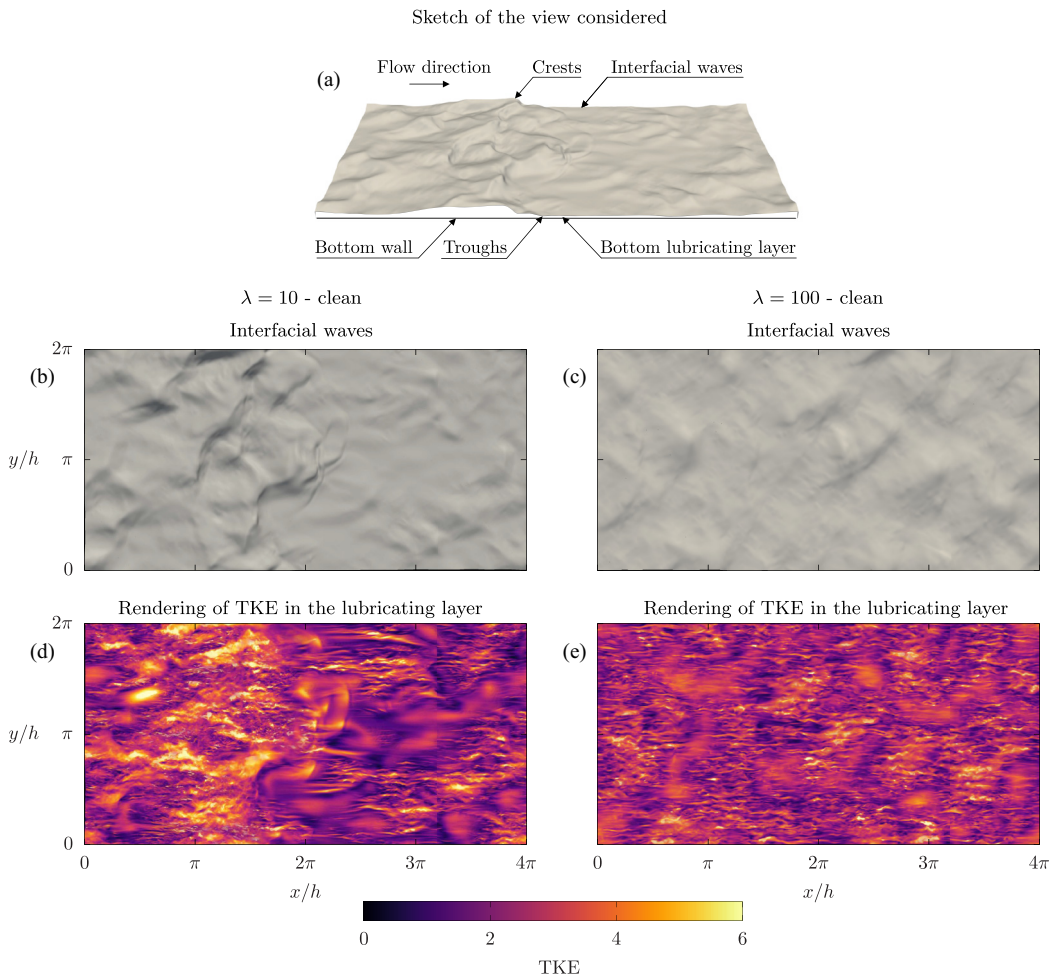
FIG. 2. Panel (a) shows a three-dimensional view of the oil-water interface near the bottom wall for the case $\lambda = 10$. The middle row shows a top view of the instantaneous deformation of the oil-water interface for the clean cases at $\lambda = 10$ (b) and $\lambda = 100$ (c), and corresponding volume rendering [(d) for $\lambda = 10$ and (e) for $\lambda = 100$] of the turbulence kinetic energy, TKE $= (u_x'^2 + u_y'^2 + u_z'^2)/2$, in the bottom lubricating layer. The flow moves from left to right and the interface shape and volume rendering of TKE are shown at the same time instant.

definition of the interface elevation is sketched in the inset of Fig. 3, using the lubricating layer near the bottom wall as reference. We recall here that the interface deformation is controlled by the interplay between the destabilizing effect of shear and turbulence and the stabilizing effect of surface tension and viscosity (since there is no density difference between the oil and water phases). Results, obtained considering the oil-water interface near both the top and the bottom walls, are shown in Fig. 3. The location of the walls is explicitly indicated (hatched box at $\zeta/h = -0.15$ on the left of the picture). Positive values of ζ/h indicate interface crests, whereas negative values of ζ/h indicate interface troughs (see the inset). The different cases are reported with different colors: violet for $\lambda = 10$ and red for $\lambda = 100$. Continuous and dashed lines are used to identify the clean and surfactant-laden cases, respectively. We immediately notice that the shape of the PDFs strongly depends on the considered viscosity ratio. For $\lambda = 10$ (violet), the PDF has a peak at $\zeta/h \simeq -0.07$, indicating that the interface preferentially deforms towards the wall, with interface
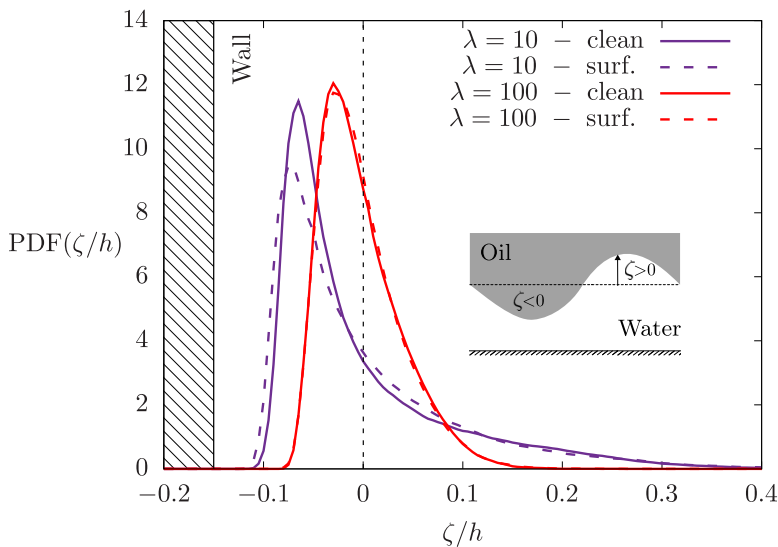
FIG. 3. Probability density function (PDF) of interface elevation, ζ/h. Positive values of ζ/h identify interface crests: Locations where the interface is above the average interface position (i.e., located towards the center of the channel). Negative values of ζ/h indicate interface troughs: locations where the interface is below the average interface position (i.e., close to the wall). The reference system used to define crests and troughs is also shown in the inset. Results that refer to $\lambda = 10$ are reported with violet lines while those referring to $\lambda = 100$ with red lines. Clean cases are reported with continuous lines while surfactant-laden cases with dashed lines.

troughs that can get rather close to the bottom wall, reducing the instantaneous thickness of the lubricating layer and therefore promoting the local flow laminarization [as already discussed, see laminar patches in Fig. 2(b)]. We also notice that the PDF is positively skewed, suggesting that large positive fluctuations of the interface elevation are more likely to occur than large negative fluctuations. This is an effect of the wall confinement, which limits the amplitude of the negative fluctuations (trough close to the wall) but not of the positive fluctuations (crests far from the wall). Moving to the case $\lambda = 100$, we observe that, compared to the case $\lambda = 10$, the peak of the PDF is at $\zeta/h \simeq -0.03$, i.e., closer to the reference interface position and that the shape of the PDF is less skewed. This indicates that waves are smaller in amplitude and therefore less influenced by the presence of the wall. This is consistent with the qualitative results shown in Fig. 2(e), where turbulence activity was rather uniform in the lubricating layer. The different behavior observed for $\lambda = 10$ and $\lambda = 100$ is due to the interaction between the surface tension forces and the oil viscosity. In particular, unlike the case $\lambda = 10$, where the viscosity ratio—and therefore the oil viscosity—is not so large to play a significant role, for $\lambda = 100$, the oil viscosity is large enough to effectively damp the interface deformation. This means that an increase of oil viscosity decreases the interface deformation, very much like an increase of surface tension does.

We now focus on the influence of surfactants. For $\lambda = 10$, the presence of the surfactant slightly modifies the shape of the PDF, making it even more positively skewed. In this case, the surfactant acts on an interface that is already rather deformable and further increases its deformability (reducing surface tension). This induces a slight increase of rare negative events and a corresponding shift of the PDF peak towards the wall (i.e., the interface can be closer to the wall). Moderate positive interface elevations are also slightly increased ($0 < \zeta/h < 0.1$). For $\lambda = 100$, the difference between the clean and surfactant-laden case is negligible. This is mostly due to the effect of viscosity: Viscous forces stabilize the interface and balance the surface tension reduction induced by the presence of surfactants.
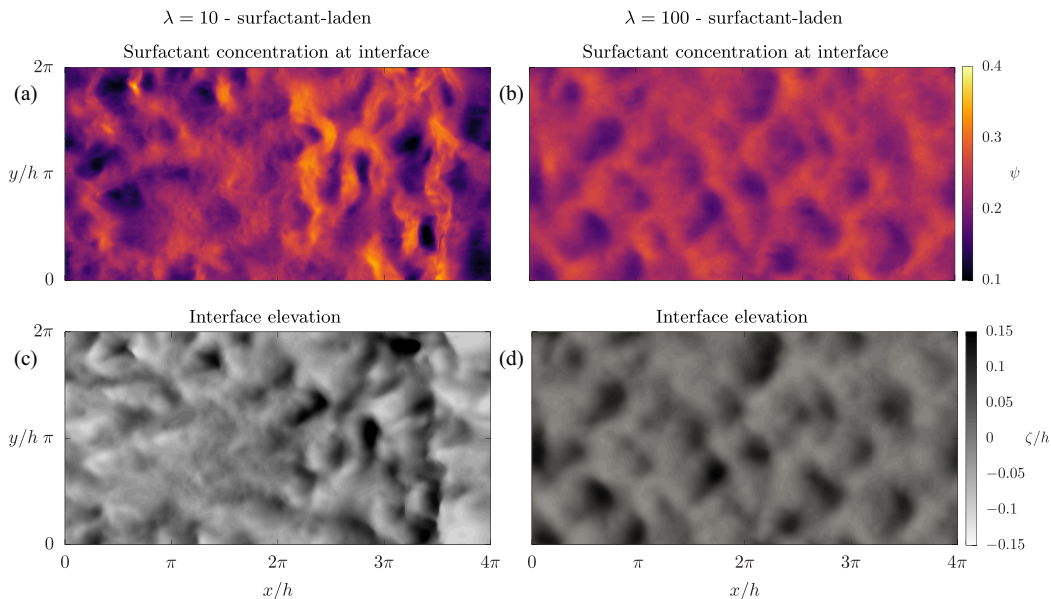
FIG. 4. Surfactant concentration (top row, dark-low; light-high) and interface elevation (bottom row, dark-crests; white-troughs) for the different cases considered. The left column refers to $\lambda = 10$ while the right column to $\lambda = 100$. Higher surfactant concentrations are obtained in proximity of interface troughs (negative values of ζ/h, interface regions close to one of the walls) while lower surfactant concentrations are found close to interface crests (positive values of ζ/h, interface regions far from the walls).

The differences observed in the interface structure between the clean and surfactant-laden cases, can be better understood by looking at the surfactant distribution at the interface, i.e., at $\phi = 0$. Figure 4 shows the instantaneous value of the surfactant concentration (top row: dark-low, light-high) together with the instantaneous value of the interface elevation ζ/h (bottom row: dark-crests, light-troughs). The left column [Figs. 4(a) and 4(c)] refers to $\lambda = 10$, while the right column [Figs. 4(b) and 4(d)] refers to $\lambda = 100$.

For $\lambda = 10$ (left column), we observe a rather uneven distribution of the surfactant at the interface: Regions having high values of the surfactant concentration, and thus strong surface tension reductions (light colors), coexist with regions having small values of the surfactant concentration, and thus smaller surface tension reductions (dark colors). A vis-à-vis comparison between Figs. 4(a) and 4(c) shows that regions characterized by small surfactant concentrations (dark colors) seem to correlate with regions characterized by large values of the interface elevation (dark colors). This correlation holds also for $\lambda = 100$ [Figs. 4(b) and 4(d)], even though waves are smaller and so are gradients of surfactant concentration.

To quantify the correlation between the interface elevation, ζ/h, and the surfactant concentration at the interface ($\phi = 0$), we compute their joint probability density function (JPDF). Results are shown in Fig. 5; Fig. 5(a) refers to $\lambda = 10$ (surfactant-laden case) while Fig. 5(b) refers to $\lambda = 100$ (surfactant-laden case). The interface elevation is shown in the x axis, while the surfactant concentration is shown in the y axis. The equilibrium surfactant concentration [obtained from Eq. (8) for $\phi = 0$] is indicated by the dashed horizontal line, whereas the mean position of the interface is indicated by the dashed vertical line. A light-dark colormap shows the probability density function.

Considering $\lambda = 10$ [Fig. 5(a)], we observe that for negative values of the interface elevation (troughs), the surfactant distribution is rather wide, indicating that the high-concentration region and low-concentration region are found inside the troughs (no clear correlation between the interface elevation and the surfactant concentration). As we move towards larger values of the interface
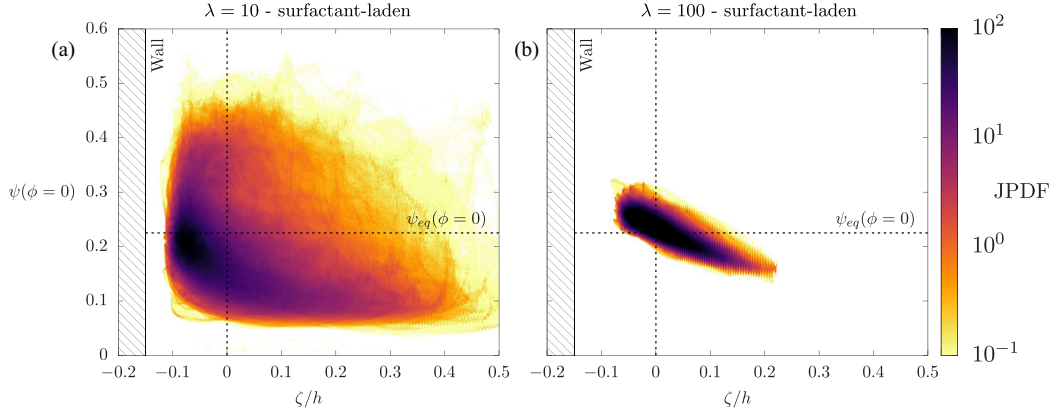
FIG. 5. Joint probability density functions (JPDF) of surfactant concentration (evaluated at the interface position, $\phi = 0$) and interface elevation ζ/h. The equilibrium value of the surfactant concentration (at $\phi = 0$) is reported with a dashed horizontal line, while the mean interface position ζ/h is reported with a vertical dashed line. Panel (a) refers to $\lambda = 10$ while panel (b) to $\lambda = 100$. A light-dark colormap is used to identify contours of the probability density function.

elevation (crests), the picture changes, and the distribution is no longer centered about the surfactant equilibrium concentration. In particular, for large values of interface elevation ($\zeta/h > 0.15$), low values of the surfactant concentration are more likely observed ($\psi \simeq 0.1$). This indicates the tendency for surfactants to leave the crests and accumulate into troughs. As a consequence, crests are characterized by small surface tension modifications (small surfactant concentration), while troughs are characterized by large surface tension modifications (large surfactant concentration). This observation provides also a possible explanation for the different behavior of PDF(ζ/h) (see Fig. 3) for negative (troughs) and positive (crests) events in case of a surfactant-laden system. Indeed, most of the modifications are observed in the region corresponding to interface troughs, where surfactant accumulates. Considering now $\lambda = 100$ [Fig. 6(b)], the distributions of surfactant
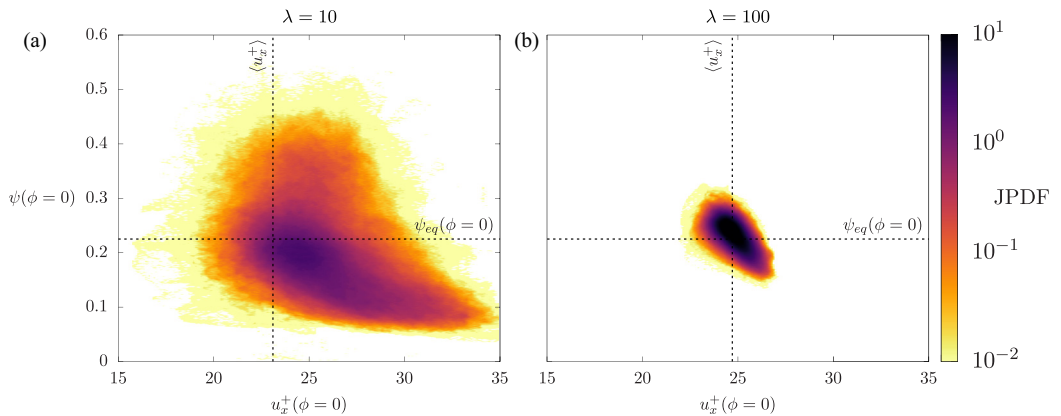

FIG. 6. Joint probability density functions (JPDF) of the surfactant concentration and the instantaneous interface velocity. Both quantities are evaluated at the interface position $\phi = 0$. The equilibrium value of the surfactant concentration at $\phi = 0$ is shown by a dashed horizontal line. The mean velocity at the interface position, $\langle u_x^+(z/h = \pm 0.85)\rangle$, is shown by a vertical dashed line. Panel (a) refers to $\lambda = 10$ while panel (b) to $\lambda = 100$.

concentration and interface elevation become narrow, but the trend remains similar to the previous case, and even more clear: High surfactant concentrations correlate with the presence of troughs and low surfactant concentration with the presence of crests.

A possible explanation to the correlation existing between crests and low surfactant concentrations (respectively, troughs and high surfactant concentration) can be found considering the different value of the streamwise velocity near interface crests and troughs: near interface crests (far from the walls) the streamwise velocity is higher, while near interface troughs (close to the walls) the streamwise velocity is lower. Because of this relative velocity, surfactants are transported from interface crests towards interface troughs. As a result, interface crests are depleted of surfactants, which in turn accumulate at the interface troughs.

We test our conjecture computing the JPDF of the surfactant concentration, evaluated at the interface position ($\phi = 0$), and the instantaneous streamwise velocity at the interface location, $u_x^+(\phi = 0)$. Results are shown in Fig. 6 for $\lambda = 10$ [Fig. 6(a)] and $\lambda = 100$ [Fig. 6(b)]. The surfactant concentration is reported along the vertical axis, while the instantaneous streamwise velocity is reported along the horizontal axis. The equilibrium surfactant concentration is indicated by the dashed horizontal line, while the mean streamwise velocity at the interface location, $\langle u_x^+(\phi = 0) \rangle$, is indicated by a vertical dashed line. A light-dark colormap is used to identify the isocontours of the probability density function.

For the case $\lambda = 10$ [Fig. 6(a)], a negative correlation between surfactant concentration and interface velocity is observed, in particular for higher-than-mean velocity [$u_x^+ > u_x^+(\phi = 0)$] and lower-than-equilibrium surfactant concentrations ($\psi < \psi_{eq}$). This indicates that crests (regions with higher-than-mean velocity) are characterized by smaller surfactant concentrations. This correlation is less pronounced for troughs [$u_x^+ < u_x^+(\phi = 0)$], where regions of large and small surfactant concentration can be found. For the case $\lambda = 100$ [Fig. 6(b)], the distributions of the surfactant concentration becomes narrower, but the trend is similar to the one observed for $\lambda = 10$. In fact, the negative correlation between velocity and surfactant concentration is even more apparent: Crests correlate with small surfactant concentration and trough with large surfactant concentration.

B. Turbulence features and wall shear stresses

As already anticipated, the dynamics of the oil-water interface has an influence on the behavior of the flow field in the lubricating layer and in particular in the proximity of the wall. This aspect can be properly investigated by looking at the streaky structure of the flow near the bottom wall. In particular, we consider the spatial distribution of the instantaneous streamwise velocity, u_x^+, in a $x - y$ plane located at $z/h = 0.99$, i.e., at distance $0.01h$ from the wall (roughly corresponding to 10 wall units). Figure 7(a) shows the considered plane (shown in red) and its position with respect to the oil-water interface: The plane is located entirely in the bottom lubricating layer and does not intersect the deformable oil-water interface. Figures 7(b)–7(f) shows the contour map of the streamwise velocity obtained for the five different cases: single-phase [Fig. 7(b)], $\lambda = 10$ (clean) [Fig. 7(c)], $\lambda = 100$ (clean) [Fig. 7(d)], $\lambda = 10$ (surfactant-laden) [Fig. 7(e)], and $\lambda = 100$ (surfactant-laden) [Fig. 7(f)]. Dark colors indicate high velocity values, while light colors indicate low velocity values. In all panels, the flow moves from left to right along the x positive direction. Note that, because of the flow symmetry, a similar behavior would be observed near the top wall.

For the single-phase case [Fig. 7(a)], we observe the classical streaky structure of wall turbulence characterized by the presence of low-speed streaks, whose spacing scales in wall units ($l_y \sim 100$ w.u.). We also observe the footprint of large-scale motions (LSM) as highlighted by the clustering of low- or high-speed streaks with a streamwise length of $\simeq \pi h$. Considering the multiphase cases [water-lubricated channels, Figs. 7(c)–7(f)], we notice a very different flow structures. We focus first on the clean cases only, Figs. 7(c) and 7(d). For $\lambda = 10$ [Fig. 7(c)], turbulence is highly nonuniform and seems to show the typical patterns of laminar-turbulent flow transition [70,71], characterized by the coexistence of nearly laminar regions (laminar patches) and regions of very high turbulence activity (turbulence pockets or spots, with high-low speed streaks).
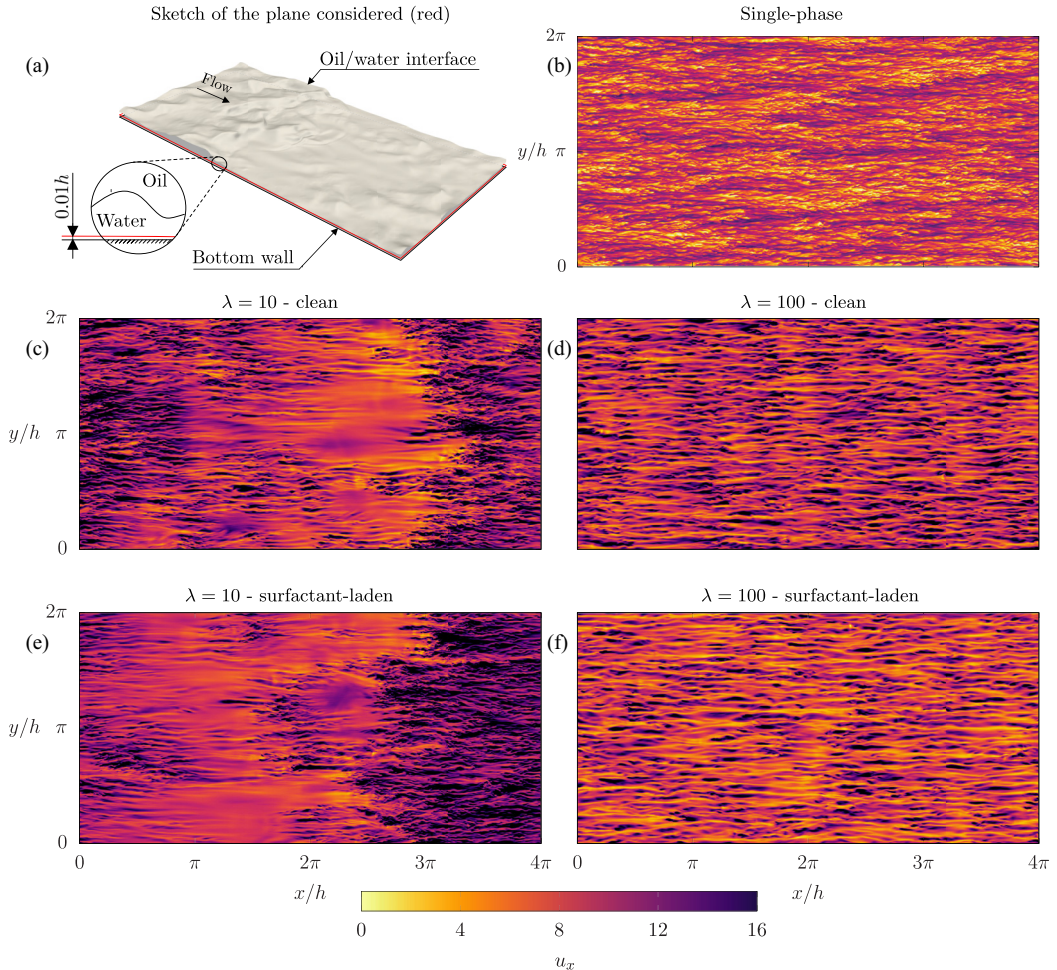
FIG. 7. Instantaneous distribution of the streamwise velocity, u_x, in a wall-parallel section ($x - y$ plane) located at a distance $d/h = 0.01$ from the bottom wall (roughly corresponding to 10 w.u.). Panel (a) shows the location of the considered $x - y$ plane: The plane is located inside the bottom lubricating layer and does not intersect the oil-water interface. Panel (b) refers to the single-phase case; panels (c) and (e) to $\lambda = 10$; and panels (d) and (f) to $\lambda = 100$. The middle row refers to the clean cases, while the bottom row to the surfactant-laden cases.

For $\lambda = 100$ [Fig. 7(d)], the situation changes, and turbulence appears reactivated and almost evenly distributed on the $x - y$ plane. In fact, the situation is different compared to the single-phase case [Fig. 7(a)]: The characteristic length scale of turbulence appears larger in the spanwise direction, and there seems to be no-signature of LSM [clustering of low- or high-speed streaks like those in Fig. 7(a)].

We look now at the influence of surfactants on the turbulence activity in the lubricating layers. For $\lambda = 10$—but similar trends, though less emphasized, are also visible at $\lambda = 100$—laminar patches are larger, and the turbulence seems a bit stronger than the clean case. This is due to the change of the interface position, which comes closer to the wall when surfactants are present (see Fig. 3).

To characterize the different turbulence structure observed in the lubricating layers, we look at the wall shear stress, and we compute its PDF [38,40,72–75]. Results are shown in Fig. 8. Note that, given the definition of the wall shear stress, $\tau_w = \eta_w \partial u_x / \partial z$, negative values of τ_w represent

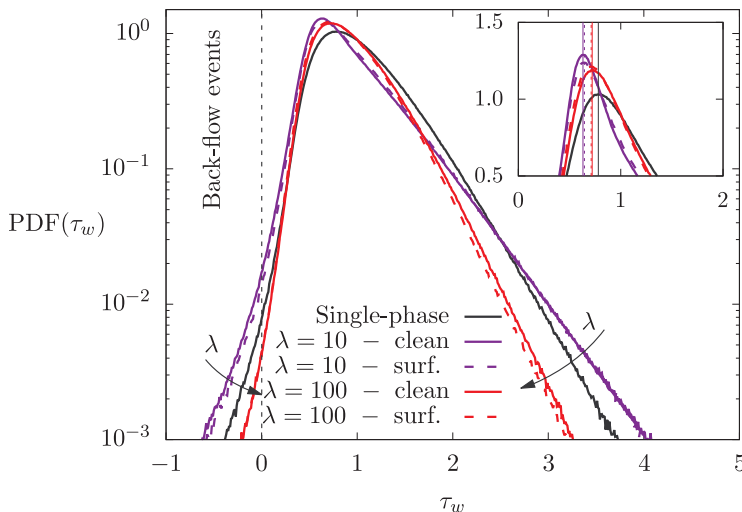FIG. 8. PDF of the wall-shear stress, τ_w. The behavior of the single-phase case is shown using a black line. Results that refer to $\lambda = 10$ are reported with violet lines while those referring to $\lambda = 100$ with red lines. Clean cases are reported with continuous lines while surfactant-laden cases with dashed lines. A dashed vertical line indicates the critical condition $\tau_w = 0$. The inset shows the PDFs in linear scale and vertical lines (same color code) are used to mark the location of the PDF peak.

back-flow events, i.e., flow regions where velocity goes against the mean pressure gradient (i.e., against the mean flow velocity) [38,74,76].

The different cases in Fig. 8 are identified by different colors: black for the single-phase flow, violet for $\lambda = 10$, and red for $\lambda = 100$. Continuous and dashed lines are used for the clean and surfactant-laden cases, respectively. A dashed vertical line highlights the critical condition $\tau_w = 0$ and the region where back-flow events occur. First, we focus on the single-phase case. In agreement with previous literature studies [38,72–75], we notice that the PDF(τ_w) is asymmetric and positively skewed, indicating that positive fluctuations are larger in magnitude and occur more frequently than negative fluctuations (the maximum value is $\tau_w \simeq 4$, while the minimum is $\tau_w \simeq -0.5$). The probability of observing negative events, despite being smaller than that of positive events, is non-negligible and is found to increase for increasing Reynolds numbers [74].

The situation changes for the multiphase flow cases. For $\lambda = 10$ (violet lines), there is an increased probability not only of large positive and negative τ_w but also of intermediate events, $0 < \tau_w < 1$, as clearly shown in the inset of Fig. 8. All these results are due to the modulation of the wall-shear stress by the interface deformation. When the interface has a crest, there is room for the flow in the lubricating layer to sustain and amplify turbulence fluctuations (i.e., larger probability of $\tau_w < 0$ and $\tau_w > 3$). When the interface has a trough, there is no room for turbulence to develop in the lubricating layer, and the flow becomes laminar. This explains the larger probability of observing nearly laminar shear stress ($0 < \tau_w < 1$).

The correlation between interface deformation (crests and troughs) and the wall-shear stress is shown for $\lambda = 10$ in Fig. 9(a): Isocontours (white) of the interface elevation highlighting crests and troughs are superposed to the contour maps of the wall-shear stress. It is clear that when the interface is close to the wall ($\zeta/h < 0$, troughs), laminar patches are present and these patches are characterized by $\tau_w \simeq 0.5$ (orange). When the interface is far from the wall ($\zeta/h > 0$, crests), turbulence pockets appear, as highlighted by the fluctuations of the wall-shear stress (light to dark colors).

Moving now to the case $\lambda = 100$ (red lines) in Fig. 8, the picture changes compared to the case $\lambda = 10$, and the PDF becomes closer to the PDF of the single-phase case (though with a reduction of
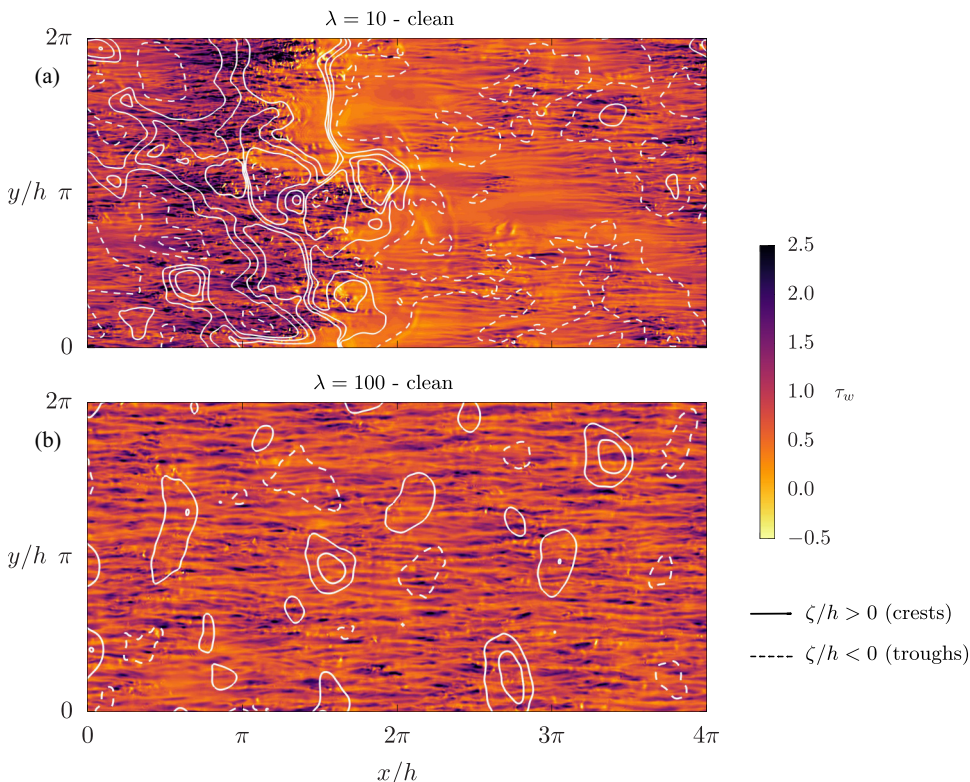
FIG. 9. Superposition of contour maps of the wall-shear stress at the bottom wall (colors, white-low; dark-high) and isocontours (white) of the interface elevation ζ/h. For the interface elevation, continuous lines identify positive interface elevations (crest) while dashed lines identify negative values (troughs). Panel (a) refers to $\lambda = 10$ while panel (b) to $\lambda = 100$. For $\lambda = 10$, positive values of the interface elevations ζ/h (continuous lines) correlate with large positive and negative fluctuations of the wall-shear stress, while negative values of the interface elevation ζ/h (dashed lines) correlate with low values of the wall-shear stress (laminar patches). For $\lambda = 100$ this correlation is not present, and the wall-shear stress distribution is more uniform.

the probability to observe extreme positive and negative events—because of the absence of LSM—and slightly larger probability of observing moderate events, $0.5 < \tau_w < 1$. The uniform turbulence activity obtained for this case can be also appreciated from Fig. 9(b), which shows the wall-shear stress distribution at the bottom wall together with the isocontours of the interface elevation (white). It is apparent that the distribution of the wall shear stress is more uniform in the entire $x - y$ plane and that is not correlated with the interface elevation (solid and dashed white lines do not correlate with specific flow features at the wall). We finally note that the presence of surfactants induce only minor changes to the picture (see dashed lines in Fig. 8).

C. Mean velocity, flow rates, and pressure gradient

The changes in the local flow structure discussed above result into a corresponding change in the macroscopic flow properties. We start by considering the mean streamwise velocity, $\langle u_x^+ \rangle$, as a function of the wall-normal coordinate. Results are shown in Fig. 10 for the different cases: single-phase flow (black), $\lambda = 10$ (violet), and $\lambda = 100$ (red). Continuous and dashed lines refer, as usual, to the clean and surfactant-laden cases, respectively. In Fig. 10(a), velocity is expressed in wall units (using the value of u_τ evaluated for each case, see Table I) while the wall-normal
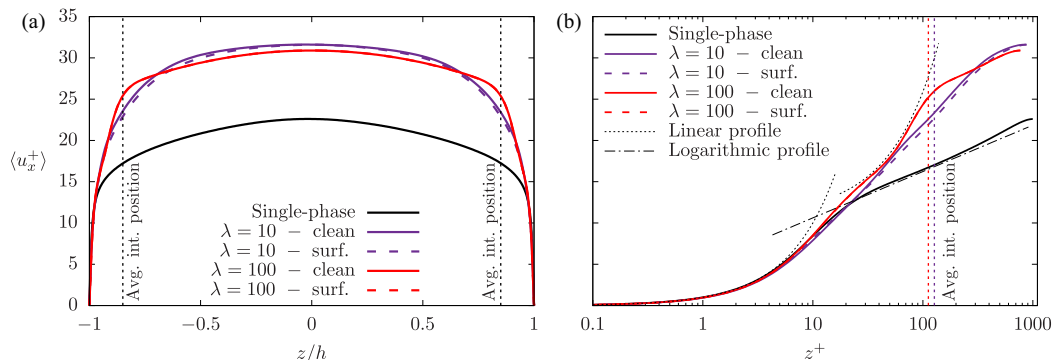
FIG. 10. Wall-normal behavior of the mean streamwise velocity, $\langle u_x^+ \rangle$. Panel (a) shows the velocity profiles in linear scale (outer units) while panel (b) in semilogarithmic scale (wall units). The different cases are reported: single-phase flow (black line), $\lambda = 10$ (violet), and $\lambda = 100$ (red). Clean cases are reported with continuous lines and surfactant-laden cases with dashed lines. Two vertical lines mark the average position of the interface, $z/h = \pm 0.85$. Linear and logarithmic profiles are also reported as a reference with thin dotted and dash-dotted lines, respectively.

coordinate is expressed in outer units, z/h. In Fig. 10(b), both velocity and wall-normal coordinates are expressed in wall units, z^+, and plotted in semilogarithmic scale (z^+ coordinate). The classical law of the wall, $u^+ = z^+$ and $u^+ = (1/k) \log(z^+) + 5.2$ (with $k = 0.41$ the von Kármán constant), is also reported as a reference [77]. The vertical dashed lines indicate the average position of the interface: In Fig. 10(a), $z/h = \pm 0.85$; in Fig. 10(b), the average position of the interface is different because of the different friction velocity.

Compared to the single phase case, and no matter the value of λ, we immediately notice that the water-lubricated channel cases are characterized by a large increase of mean velocity. Specifically, for $\lambda = 10$, we observe velocity values in the central part of the channel (oil phase), which are approximately 50% larger than those obtained for the single-phase case. For $\lambda = 100$ we observe similar results, though the shape of the velocity profile is different, in particular near the average interface position. It is interesting to note that, the larger the viscosity ratio, the flatter becomes the profile in the central region of the channel: The high oil viscosity in the core of the channel strongly reduces the velocity gradients and the turbulent fluctuations in this region. This seems to indicate that the oil layer at center of the channel moves as a plug flow, in particular for $\lambda = 100$. This aspect becomes extremely clear in Fig. 10(b). While in the near wall region—occupied by the lubricating layers—all velocity profiles match the classical law of the wall, $\langle u_x^+ \rangle = z^+$ (first dotted line), from $z^+ \sim 25$, the velocity profiles of the water-lubricated cases do depart from the logarithmic law and follow a steeper increase. In particular, for $\lambda = 100$ (red line), the velocity profile follows a linear behavior (second dotted line), closely recalling the Couette-Poiseuille flow instances [78]. The emerging picture is the following: The oil core, given its high viscosity, moves as a plug flow inside the channel, very much like the moving solid boundary does in the Couette case; this plug flow drives the motion inside the lubricating layer. Note that the presence of surfactants induces only minor changes to this picture. In fact, for $\lambda = 100$, the clean and surfactant-laden cases perfectly overlap.

We finally look at the drag reduction obtained by computing the flow rates and the pressure drop of the water-lubricated channels. Results are normalized by the corresponding single-phase flow of oil and are shown in Fig. 11. In Fig. 11(a), we plot the flow rate as a function of the applied pressure gradient, i.e., (p_x, Q_t) pairs. The black solid line indicates the value of the power (proportional to the product between p_x and Q_t), which is kept constant among all simulations (CPI approach, see Sec. II). In Fig. 11(b), we plot the behavior of the pressure gradient, p_x, and of the flow rate of the oil core and of the entire channel, Q_o and Q_t, respectively, as a function of the viscosity ratio, λ.
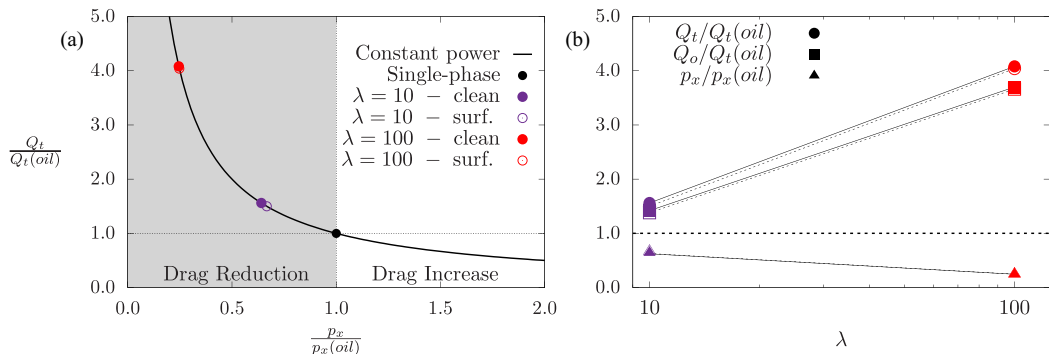
FIG. 11. Steady-state values attained by the oil flow rate, Q_o, total flow rate, Q_t, and pressure gradient p_x in physical units and normalized by the single-phase value of the corresponding oil. Panel (a) shows the achieved flow rates against the required pressure gradient; a black line is used to identify the constant power input constraint. Panel (b) shows the effect of the viscosity ratios on the flow rates and pressure gradient. Clean (surfactant-free) cases are represented with full symbols while surfactant-laden cases are shown with empty symbols. For both viscosity ratios considered, it can be observed that the oil flow rate is obtained using the water-lubricated technique is greater than that of the single-phase value of the respective oil.

Clean cases are represented by full symbols, while surfactant-laden cases are represented by empty symbols. Different colors are used to indicate different cases: $\lambda = 10$ (violet) and $\lambda = 100$ (red).

Looking at Fig. 11(a), we can first observe that all simulation data collapse on the black solid line, which represents the CPI constraint (isopower curve). Considering the various cases, we notice that the total flow rate, Q_t, is always larger than that of the single-phase flow (of the corresponding oil). In particular, for $\lambda = 10$, the oil flow rate is 1.7 times larger than that of the corresponding single-phase flow, while for $\lambda = 100$, it is 4 times larger. Since the simulations are performed keeping constant the power input, an increase of the total flow rate corresponds to a decrease of the pressure gradient applied to drive flow ($p_x \simeq 0.6$ for $\lambda = 10$, and $p_x \simeq 0.25$ for $\lambda = 100$). The presence of surfactants induces only minor differences to the overall flow rates or pressure gradients: surfactant-laden cases exhibit slightly smaller flow rates with respect to the surfactant-free counterparts. This effect is a bit more visible for $\lambda = 10$, while it vanishes for $\lambda = 100$. Overall, these results indicate that a remarkable DR is observed in water-lubricated oil channels, which clearly depends on the considered viscosity ratio between the transported fluid and the fluid used to lubricate the flow. At the same time, the presence of surfactants and impurities has only little effect on the drag reduction performances, and this effect tends to vanish when larger viscosity ratios are considered ($\lambda = 100$). Finally, it is interesting to observe that the mechanisms leading to drag reduction in the low- and high-viscosity cases are slightly different: For $\lambda = 10$, the larger amplitude of the interfacial waves leads to the generation of laminar patches, which induce lower strain rates and, together with the smaller water viscosity, leads to drag reduction. This DR mechanism resembles the one observed in our previous works [38,39] performed at moderate viscosity ratios with a single lubricating layer where turbulence-interface interactions are the main factor leading to DR. For $\lambda = 100$, the former drag reduction mechanism (generation of laminar patches) tends to vanish, and drag reduction is mainly driven by the small viscosity of the lubricating layer (water). Hence, compared to previous works [38,39], the observed DR mechanism is different and is mainly linked to the low viscosity of the lubricating layer.

IV. CONCLUSIONS

We have performed direct numerical simulations of a water-lubricated channel flow, a flow instance in which two near-wall thin lubricating layers of water are used to favor the transport

of a more viscous fluid (e.g., oil). The simulations rely on DNS of turbulence, coupled with a phase-field method, which is used to describe the dynamics of the oil-water interface and the presence of surfactants or contaminants. Simulations have been performed using the CPI approach. We considered a channel geometry, and by keeping the viscosity of the two lubricating layers fixed (e.g., assuming water as lubricating fluid), we considered two different types of oil: an oil that is 10 times more viscous than the water of the lubricating layer (viscosity ratio $\lambda = \eta_o/\eta_w = 10$) and an oil that is 100 times more viscous (viscosity ratio $\lambda = 100$). For each value of the viscosity ratio, a clean (surfactant-free) case—characterized by a constant and uniform value of the surface tension—and a surfactant-laden case—characterized by a surface tension value that depends on the local surfactant concentration—have been studied.

First, we analyzed the interplay between the interface deformation and the turbulence activity in the two lubricating layers. For $\lambda = 10$, we observed large interface deformations, which are larger towards the channel center than towards the wall (wall-confinement effect). Therefore, the interface strongly interacts with the near-wall turbulence cycle: laminar regions appear where the interface is close to the wall (and there is not enough room in the lubricating layer to develop and sustain turbulence), while turbulence regions appear where the interface is farther from the wall. Naturally, this induces large fluctuations of the wall-shear stress τ_w. For $\lambda = 100$, the large oil viscosity acts as a stabilizing agent to the interface, which becomes less deformable. As a result, the interface deformations are smaller in magnitude and almost symmetric (there is only a slight asymmetry between deformations towards the channel center and deformations towards the wall). This reduces the interactions between the near-wall turbulence cycle and the interface itself: laminar patches are no longer present near the wall, and instead a rather uniform turbulence activity can be observed in the two lubricating layers. For both cases, the addition of a surfactant is found to have little effect, with more pronounced modifications observed for $\lambda = 10$. However, further investigations are required to confirm present findings: surfactant dynamic is controlled by many different parameters (e.g., strength, diffusivity, adsorption or desorption, solubility).

Finally, we considered the behavior of the macroscopic flow parameters. We observed that the mean velocity profiles follows the classical law of the wall up to $z^+ < 30$ w.u. in the two lubricating layers. For larger values of the wall-normal coordinate, the profiles deviate from the logarithmic law, not only because of the presence of the interface, but also because of the pluglike flow of oil at the core of the channel (due to the high oil viscosity). Considering the drag reduction performance, we observe that oils, 10 and 100 times more viscous than water, can be transported appling a remarkable lower pressure gradient, p_x. Specifically, compared to the corresponding single phase of oil, we observed a reduction down to $p_x/p_{x,\mathrm{sp}} \simeq 0.25$ for $\lambda = 100$. Present results highlight the potential of the water-lubricated technique in effectively reducing the drag and thus favoring the transport of highly viscous fluids. However, further studies are required before applying this technique in industrial configurations as one limitation of the present work is the moderate Reynolds number considered (due to the computational requirements of DNS of multiphase turbulence).

APPENDIX: EXTENSION OF THE CPI APPROACH TO VISCOSITY STRATIFIED MULTIPHASE FLOWS

We present here the extension of the CPI approach to viscosity stratified flows. We start by briefly summarizing its derivation for a single-phase flow [46,56]. In particular, we consider the flow inside a plane channel bounded by two walls located at $z = \pm h$, Fig. 12(a). The flow is Newtonian, with viscosity η. A constant pumping power per unit area, P_p, is used to drive the flow along the
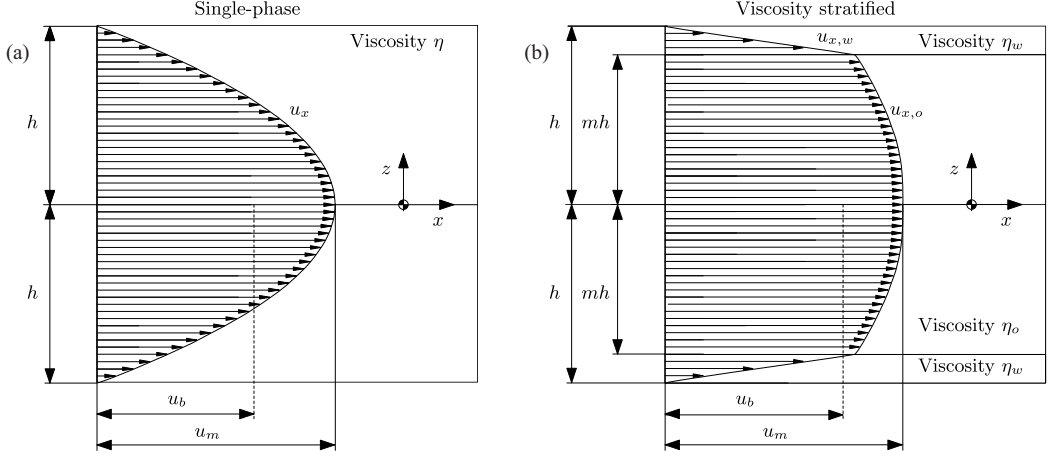
FIG. 12. Sketch of the channel configurations used to derive the laminar flow solution: single phase (a) and viscosity stratified (b). For the single phase, the viscosity, η, is uniform and thus a symmetric velocity profile, u_x, is obtained. For the viscosity stratified case, the thin lubricating layer ($mh < z < h$) has viscosity η_w while the primary layer ($-h < z < mh$) has viscosity η_o and an asymmetric velocity profile ($u_{x,w}$ in the lubricating layer and $u_{x,o}$ in the primary layer) is obtained. For both panels, the maximum velocity, u_m, and the bulk velocity, u_b, have been highlighted.

streamwise direction. Assuming a laminar flow, the following velocity profile is obtained:

$$u_x(z) = \frac{1}{2\eta}(z^2 - h^2), \tag{A1}$$

where p_x is the pressure gradient along the streamwise direction. The bulk velocity (i.e., the average velocity across the channel section) can be computed integrating the velocity profile along the wall-normal direction:

$$u_b = \frac{1}{2h}\int_{z=-h}^{z=h} u_x dz = \frac{1}{3\eta}(-p_x)h^2. \tag{A2}$$

The power dissipated by the viscous forces can be computed as:

$$\epsilon = \frac{1}{2}\int_{z=-h}^{z=h}\eta\left(\frac{du_x}{dz}\right)^2 dz = \frac{1}{\eta}(p_x)^2\frac{h^3}{3} = \frac{3\eta}{h}\underbrace{(p_x)^2\frac{h^4}{9\eta^2}}_{u_b^2} = \frac{3\eta u_b^2}{h}, \tag{A3}$$

At equilibrium (i.e., fully developed flow), the power dissipated by the viscous forces is equal to the power injected in the system. Matching the expression of P_p with Eq. (A3), we can identify a velocity scale, u_Π, for the problem:

$$u_b = u_\Pi = u_\Pi^{\text{sp}} = \sqrt{\frac{P_p h}{3\eta}}. \tag{A4}$$

To extend the CPI approach to viscosity stratified flows, we can proceed in a similar way. We refer to the sketch in Fig. 12(b). The top and bottom lubricating layers are characterized by viscosity η_w while the central layer is characterized by viscosity η_o. The flow is laminar and the interface between the two layers is located at $z = \pm mh$ (note that $m = 0.85$ in the present work). No-slip boundary conditions are applied at the two walls, while continuity of velocity and stress is enforced at the

interface [79, p. 198]. The resulting streamwise velocity profile is

$$u_x(z) = \begin{cases} u_{x,w}(z) & \text{for} \quad mh < z < h \\ u_{x,o}(z) & \text{for} \quad -mh < z < mh \\ u_{x,w}(z) & \text{for} \quad -h < z < -mh \end{cases}, \tag{A5}$$

where $u_{x,w}$ is the velocity in the two lubricating layers and $u_{x,o}$ is the velocity profile in the core layer. These two velocities are defined as follows:

$$u_{x,w}(z) = \frac{1}{2\eta_w}(p_x)(z^2 - h^2), \tag{A6}$$

$$u_{x,o}(z) = \frac{1}{2\eta_o}(p_x)(z^2 - Ah^2), \tag{A7}$$

where the coefficient A, which depends on the thickness of the lubricating layer (i.e., on the parameter m) and on the viscosity ratio $\lambda = \eta_o/\eta_w$, is defined as:

$$A(\lambda, m) = \lambda - \lambda m^2 + m^2. \tag{A8}$$

The bulk velocity can be computed integrating the velocity profile along the wall-normal direction (i.e., the two velocity profiles over the corresponding thickness). Using the symmetry of the system, we can write:

$$u_b = \frac{1}{h}\left[\int_{z=mh}^{z=h} u_{x,w}dz + \int_{z=mh}^{z=0} u_{x,o}dz \right] = \frac{1}{\eta_1}(-p_x)\frac{h^2}{3}B, \tag{A9}$$

where the coefficient B is defined as:

$$B = 1 - \frac{3}{2}m + \frac{m^3}{2} - \frac{m^3}{2\lambda} + \frac{3mA}{2\lambda}. \tag{A10}$$

The coefficient B highlights the main difference with the expression of the bulk velocity for a single-phase flow [Eq. (A2)]. From a physical point of view, the ratio η_w/B can be interpreted as the equivalent viscosity of the system.

Similarly, the power dissipated by the viscous forces can be computed from the expression of the velocity profiles:

$$\epsilon = \left[\int_{z=mh}^{z=h} \eta_w \left(\frac{du_{x,w}}{dz} \right)^2 dz + \int_{z=0}^{z=mh} \eta_o \left(\frac{du_{x,o}}{dz} \right)^2 dz \right]. \tag{A11}$$

After some algebra, we can simplify the expression as follows:

$$\epsilon = \frac{1}{\eta_w}(p_x)^2 h^3 D, \tag{A12}$$

where the coefficient D is defined as:

$$D = 1 - m^3 + \frac{m^3}{\lambda}. \tag{A13}$$

Viscous dissipation can be rewritten as:

$$\epsilon = \frac{3\eta_w}{h}\frac{D}{B^2} \underbrace{(-p_x)^2 \frac{h^4}{9\eta_w^2}B^2}_{u_b^2}. \tag{A14}$$

Consistently with the previous derivation, the bulk velocity is used as reference velocity scale and its expression can be obtained by matching the expression of the viscous dissipation [Eq. (A14)]

with that of the pumping power. This gives:

$$u_\Pi = u_b = \sqrt{\frac{B^2}{D}\frac{P_p h}{3\eta_w}} = \sqrt{\frac{B^2}{D}}\underbrace{\sqrt{\frac{P_p h}{3\eta_w}}}_{u_\Pi^{sp}}. \tag{A15}$$

Under CPI conditions, the coefficient $\sqrt{B^2/D}$ is used to account for the presence of two lubricating layers of different viscosity near the two walls [Eq. (A4)]. Thanks to the symmetry of the system, it is worth to observe that, on substitution of the expression of Eq. (A8) in Eq. (A10), we have $B = D$ and Eq. (A15) can be rewritten as follows:

$$u_\Pi = \sqrt{D}\sqrt{\frac{P_p h}{3\eta_w}} = \sqrt{D}u_\Pi^{sp} \tag{A16}$$

[1] A. Hart, A review of technologies for transporting heavy crude oil and bitumen via pipelines, J. Pet. Explor. Prod. Technol. **4**, 327 (2014).

[2] F. Forrest and G. Grierson, Friction losses in cast iron pipe carrying paper stock, Pap. Trade J. **92**, 39 (1931).

[3] B. A. Toms, Some observations on the flow of linear polymersolutions through straight tubes at large reynolds numbers, in *Proceedings of the 1st International Congress on Rheology* (North Holland, Amsterdam, 1948), Vol. 2, p. 135.

[4] P. S. Virk, Drag reduction fundamentals, AIChE J. **21**, 625 (1975).

[5] P. S. Virk, E. Merrill, H. Mickley, K. Smith, and E. Mollo-Christensen, The toms phenomenon: Turbulent pipe flow of dilute polymer solutions, J. Fluid Mech. **30**, 305 (1967).

[6] Y. Wang, B. Yu, J. L. Zakin, and H. Shi, Review on drag reduction and its heat transfer by additives, Adv. Mech. Eng. **3**, 478749 (2011).

[7] N. S. Berman, Drag reduction by polymers, Annu. Rev. Fluid Mech. **10**, 47 (1978).

[8] C. M. White and M. G. Mungal, Mechanics and prediction of turbulent drag reduction with polymer additives, Annu. Rev. Fluid Mech. **40**, 235 (2008).

[9] R. S. Sharma, Drag reduction by fibers, Can J. Chem. Eng. J. **59**, 3 (1981).

[10] J. Gillissen, B. Boersma, P. Mortensen, and H. Andersson, Fibre-induced drag reduction, J. Fluid Mech. **602**, 209 (2008).

[11] M. Quadrio, P. Ricco, and C. Viotti, Streamwise-travelling waves of spanwise wall velocity for turbulent drag reduction, J. Fluid Mech. **627**, 161 (2009).

[12] P. Ricco, M. Skote, and M. A. Leschziner, A review of turbulent skin-friction drag reduction by near-wall transverse forcing, Progr. Aerosp. Sci. **123**, 100713 (2021).

[13] A. Rouhi, M. K. Fu, D. Chandran, A. Zampiron, A. J. Smits, and I. Marusic, Turbulent drag reduction by spanwise wall forcing. part 1. large-eddy simulations, J. Fluid Mech. **968**, A6 (2023).

[14] R. García-Mayoral and J. Jiménez, Drag reduction by riblets, Philos. Trans. R. Soc. A **369**, 1412 (2011).

[15] M. Xu, A. Grabowski, N. Yu, G. Kerezyte, J.-W. Lee, B. R. Pfeifer, and C.-J. Kim, Superhydrophobic drag reduction for turbulent flows in open water, Phys. Rev. Appl. **13**, 034056 (2020).

[16] D. Modesti, S. Endrikat, N. Hutchins, and D. Chung, Dispersive stresses in turbulent flow over riblets, J. Fluid Mech. **917**, A55 (2021).

[17] D. Joseph, M. Renardy, and Y. Renardy, Instability of the flow of two immiscible liquids with different viscosities in a pipe, J. Fluid Mech. **141**, 309 (1984).

[18] H. Hu, T. Lundgren, and D. Joseph, Stability of core-annular flow with a small viscosity ratio, Phys. Fluids **2**, 1945 (1990).

[19] D. Joseph, R. Bai, K. Chen, and Y. Renardy, Core-annular flows, Annu. Rev. Fluid Mech. **29**, 65 (1997).

[20] S. Ghosh, T. Mandal, and P. Das, Review of oil water core annular flow, Renew. Sust. Energy Rev. **13**, 1957 (2009).

[21] C. Yih, Instability due to viscosity stratification, J. Fluid Mech. **27**, 337 (1967).

[22] C. Hickox, Instability due to viscosity and density stratification in axisymmetric pipe flow, Phys. Fluids **14**, 251 (1971).

[23] A. Hooper and W. Boyd, Shear-flow instability at the interface between two viscous fluids, J. Fluid Mech. **128**, 507 (1983).

[24] R. Oliemans, G. Ooms, H. Wu, and A. Duijvestijn, Core-annular oil/water flow: The turbulent-lubricating-film model and measurements in a 5 cm pipe loop, Int. J. Multiphase Flow **13**, 23 (1987).

[25] R. Bai, K. Chen, and D. D. Joseph, Lubricated pipelining: stability of core-annular flow. Part 5. Experiments and comparison with theory, J. Fluid Mech. **240**, 97 (1992).

[26] M. Arney, R. Bai, E. Guevara, D. Joseph, and K. Liu, Friction factor and holdup studies for lubricated pipelining-I. Experiments and correlations, Int. J. Multiphase Flow **19**, 1061 (1993).

[27] A. Bannwart, Modeling aspects of oil–water core–annular flows, J. Petrol. Sci. Eng. **32**, 127 (2001).

[28] N. Reinecke, G. Petritsch, D. Schmitz, and D. Mewes, Tomographic measurement techniques–visualization of multiphase flows, Chem. Eng. Technol. **21**, 7 (1998).

[29] R. Lindken, L. Gui, and W. Merzkirch, Velocity measurements in multiphase flow by means of particle image velocimetry, Chem. Eng. Technol. **22**, 202 (1999).

[30] T. Heindel, A review of x-ray flow visualization with applications to multiphase flows, J. Fluids Eng. **133**, 074001 (2011).

[31] S. Elghobashi, Direct numerical simulation of turbulent flows laden with droplets or bubbles, Annu. Rev. Fluid Mech. **51**, 217 (2019).

[32] G. Soligo, A. Roccon, and A. Soldati, Turbulent flows with drops and bubbles: What numerical simulations can tell us—Freeman scholar lecture, ASME J. Fluids Eng. **143**, 080801 (2021).

[33] A. Roccon, F. Zonta, and A. Soldati, Phase-field modeling of complex interface dynamics in drop-laden turbulence, Phys. Rev. Fluids **8**, 090501 (2023).

[34] K. Kim and H. Choi, Direct numerical simulation of a turbulent core-annular flow with water-lubricated high viscosity oil in a vertical pipe, J. Fluid Mech. **849**, 419 (2018).

[35] B. Song, C. Plana, J. M. Lopez, and M. Avila, Phase-field simulation of core-annular pipe flow, Int. J. Multiphase Flow **117**, 14 (2019).

[36] C. Plana, B. Song, and M. Avila, Direct numerical simulation of two-phase pipe flow: Influence of the domain length on the flow regime, Int. J. Multiphase Flow **144**, 103786 (2021).

[37] A. Alati and E. De Angelis, Turbulent statistics and interface dynamics in a lubricated channel flow at $Re_\tau = 100$, Meccanica **58**, 1959 (2023).

[38] A. Roccon, F. Zonta, and A. Soldati, Turbulent drag reduction by compliant lubricating layer, J. Fluid Mech. **863**, R1 (2019).

[39] A. Roccon, F. Zonta, and A. Soldati, Energy balance in lubricated drag-reduced turbulent channel flow, J. Fluid Mech. **911**, A37 (2021).

[40] S. Ahmadi, A. Roccon, F. Zonta, and A. Soldati, Turbulent drag reduction by a near wall surface tension active interface, Flow, Turbul. Combust. **100**, 979 (2018).

[41] S. Ahmadi, A. Roccon, F. Zonta, and A. Soldati, Turbulent drag reduction in channel flow with viscosity stratified fluids, Comput. Fluids **176**, 260 (2018).

[42] V. Badalassi, H. Ceniceros, and S. Banerjee, Computation of multiphase systems with phase field models, J. Comput. Phys. **190**, 371 (2003).

[43] D. Jacqmin, Calculation of two-phase Navier–Stokes flows using phase-field modelling, J. Comput. Phys. **155**, 96 (1999).

[44] A. Roccon, M. De Paoli, F. Zonta, and A. Soldati, Viscosity-modulated breakup and coalescence of large drops in bounded turbulence, Phys. Rev. Fluids **2**, 083603 (2017).

[45] G. Soligo, A. Roccon, and A. Soldati, Coalescence of surfactant-laden drops by phase field method, J. Comput. Phys. **376**, 1292 (2019).

[46] Y. Hasegawa, M. Quadrio, and B. Frohnapfel, Numerical simulation of turbulent duct flows with constant power input, J. Fluid Mech. **750**, 191 (2014).

[47] M. Laradji, H. Guo, M. Grant, and M. Zuckermann, The effect of surfactants on the dynamics of phase separation, J. Phys.: Condens. Matter **4**, 6715 (1992).

[48] S. Komura and H. Kodama, Two-order-parameter model for an oil-water-surfactant system, Phys. Rev. E **55**, 1722 (1997).

[49] G. Soligo, A. Roccon, and A. Soldati, Breakage, coalescence and size distribution of surfactant-laden droplets in turbulent flow, J. Fluid Mech. **881**, 244 (2019).

[50] A. Yun, Y. Li, and J. Kim, A new phase-field model for a water-oil-surfactant system, Appl. Math. Comput. **229**, 422 (2014).

[51] D. Korteweg, Sur la forme que prennent les equations du mouvements des fluides si l'on tient compte des forces capillaires causées par des variations de densité considérables mais continues et sur la théorie de la capillarité dans l'hypothèse d'une variation continue de la densité, Arch. Néerland. Sci. Exact. Natur. **6**, 1 (1901).

[52] D. López-Díaz, I. García-Mateos, and M. Velázquez, Surface properties of mixed monolayers of sulfobetaines and ionic surfactants, J. Colloid Interface Sci. **299**, 858 (2006).

[53] H. Ju, Y. Jiang, T. Geng, Y. Wang, and C. Zhang, Equilibrium and dynamic surface tension of quaternary ammonium salts with different hydrocarbon chain length of counterions, J. Mol. Liq. **225**, 606 (2017).

[54] C. Chang and E. Franses, Adsorption dynamics of surfactants at the air/water interface: a critical review of mathematical models, data, and mechanisms, Colloids Surf. A **100**, 1 (1995).

[55] M. R. Porter, *Handbook of Surfactants* (Springer Science+Business Media, New York, 1991).

[56] D. Gatti, A. Cimarelli, Y. Hasegawa, B. Frohnapfel, and M. Quadrio, Global energy fluxes in turbulent channels with flow control, J. Fluid Mech. **857**, 345 (2018).

[57] J. Kim, P. Moin, and R. Moser, Turbulence statistics in fully developed channel flow at low Reynolds number, J. Fluid Mech. **177**, 133 (1987).

[58] C. Speziale, On the advantages of the vorticity-velocity formulation of the equations of fluid dynamics, J. Comput. Phys. **73**, 476 (1987).

[59] F. Zonta, C. Marchioli, and A. Soldati, Modulation of turbulence in forced convection by temperature-dependent viscosity, J. Fluid Mech. **697**, 150 (2012).

[60] P. Yue, C. Zhou, and J. Feng, Spontaneous shrinkage of drops and mass conservation in phase-field simulations, J. Comput. Phys. **223**, 1 (2007).

[61] G. Soligo, A. Roccon, and A. Soldati, Mass-conservation-improved phase field methods for turbulent multiphase flow simulation, Acta Mech. **230**, 683 (2019).

[62] M. Kwakkel, M. Fernandino, and C. A. Dorao, A redefined energy functional to prevent mass loss in phase-field methods, AIP Adv. **10**, 065124 (2020).

[63] P. Than, L. Preziosi, D. Joseph, and M. Arney, Measurement of interfacial tension between immiscible liquids with the spinning road tensiometer, J. Colloid Interface Sci. **124**, 552 (1988).

[64] P. Yue, J. Feng, C. Liu, and J. Shen, A diffuse-interface method for simulating two-phase flows of complex fluids, J. Fluid Mech. **515**, 293 (1999).

[65] R. Weinheimer, D. Fennell, and E. Cussler, Diffusion in surfactant solutions, J. Colloid Interface Sci. **80**, 357 (1981).

[66] S. Engblom, M. Do-Quang, G. Amberg, and A. Tornberg, On diffuse interface modeling and simulation of surfactants in two-phase fluid flow, Commun. Comput. Phys. **14**, 879 (2013).

[67] H. Imuetinyan, A. Agi, A. Gbadamosi, R. Junin, and J. Oseh, Oil-water interfacial tension, wettability alteration and foaming studies of natural surfactant extracted from *vernonia amygdalina*, Pet. Res. **7**, 350 (2022).

[68] G. Giamagas, F. Zonta, A. Roccon, and A. Soldati, Propagation of capillary waves in two-layer oil–water turbulent flow, J. Fluid Mech. **960**, A5 (2023).

[69] J. Jiménez and A. Pinelli, The autonomous cycle of near-wall turbulence, J. Fluid Mech. **389**, 335 (1999).

[70] X. Wu, New insights into turbulent spots, Annu. Rev. Fluid Mech. **55**, 45 (2023).

[71] M. Avila, D. Barkley, and B. Hof, Transition to turbulence in pipe flow, Annu. Rev. Fluid Mech. **55**, 575 (2023).

[72] K. Colella and W. Keith, Measurements and scaling of wall shear stress fluctuations, Exp. Fluids **34**, 253 (2003).

[73] Z. Hu, C. Morfey, and N. Sandham, Wall pressure and shear stress spectra from direct simulations of channel flow, AIAA J. **44**, 1541 (2006).

[74] P. Lenaers, Q. Li, G. Brethouwer, P. Schlatter, and R. Örlü, Rare backflow and extreme wall-normal velocity fluctuations in near-wall turbulence, Phys. Fluids **24**, 035110 (2012).

[75] C. Brücker, Evidence of rare backflow and skin-friction critical points in near-wall turbulence using micropillar imaging, Phys. Fluids **27**, 031705 (2015).

[76] C. Chin, R. Vinuesa, R. Örlü, J. Cardesa, A. Noorani, P. Schlatter, and M. Chong, Flow topology of rare back flow events and critical points in turbulent channels and toroidal pipes, in *Journal of Physics: Conference Series*, Vol. 1001 (IOP Publishing, Bristol, UK, 2018), p. 012002.

[77] S. B. Pope, *Turbulent Flows* (Cambridge University Press, Cambridge, UK, 2000).

[78] J. H. Kim and J. H. Lee, Direct numerical simulation of a turbulent couette–poiseuille flow: Turbulent statistics, Int. J. Heat Fluid Flow **72**, 288 (2018).

[79] L. Leal, *Laminar Flow and Convective Transport Processes: Scaling Principles and Asymptotic Analysis* (Butterworth-Heinemann, Boston, 1992).